

# The Edge Intensification of Eastern Pacific ITCZ Convection

HIROHIKO MASUNAGA <sup>a</sup>

<sup>a</sup> *Institute for Earth-Space Environmental Research, Nagoya University, Nagoya, Japan*

(Manuscript received 18 May 2022, in final form 28 January 2023)

**ABSTRACT:** Tropical precipitation is climatologically most intense at the heart of the intertropical convergence zone (ITCZ), but this is not always true in instantaneous snapshots. Precipitation is amplified along the ITCZ edge rather than at its center from time to time. In this study, satellite observations of column water vapor, precipitation, and radiation as well as the thermodynamic field from reanalysis data are analyzed to investigate the behavior of ITCZ convection in light of the local atmospheric energy imbalance. The analysis is focused on the eastern Pacific ITCZ, defined as the areas where column water vapor exceeds 50 mm over a specified width (typically 400–600 km) in the domain of 20°S–20°N, 180°–90°W. The events with a precipitation maximum at the southern and northern edges of the ITCZ are each averaged into composite statistics and are contrasted against the reference case with peak precipitation at the ITCZ center. The key findings are as follows. When precipitation peaks at the ITCZ center, suppressed radiative cooling forms a prominent positive peak in the diabatic forcing to the atmosphere, counteracted by an export of moist static energy (MSE) owing to a deep vertical advection and a large horizontal export of MSE. When convection develops at the ITCZ edges, to the contrary, a positive peak of the diabatic forcing is only barely present. An import of MSE owing to a shallow ascent on the ITCZ edges presumably allows an edge intensification to occur despite the weak diabatic forcing.

**KEYWORDS:** Atmosphere; Intertropical convergence zone; Convection; Satellite observations

## 1. Introduction

The intertropical convergence zone (ITCZ) is an extensive area of enhanced moisture and precipitation, characterizing the large-scale patterns of low-latitude weather. The ITCZ has been known since the early years of modern meteorology to occur preferentially in certain geographical regions (e.g., Crowe 1951). The eastern Pacific ITCZ is particularly striking in that a narrow band of the ITCZ extends from east to west all the year around on the northern side of the equator. This meridional asymmetry of the eastern Pacific ITCZ has motivated numerous studies to unveil the mechanisms behind it (e.g., Mitchell and Wallace 1992; Xie and Philander 1994; Philander et al. 1996; Li 1997; Xie 2004; Kang et al. 2008; Masunaga and L'Ecuyer 2011). All these theories are built upon air–sea interactions, while otherwise different from one another, in explaining the climatological pattern of the eastern Pacific ITCZ.

The ITCZ morphology on short time scales, on the other hand, is affected primarily by day-to-day weather disturbances. Figure 1 presents selected satellite snapshots of column water vapor (CWV) and surface precipitation from Advanced Microwave Scanning Radiometer for the Earth Observing System (AMSR-E) observations. The eastern Pacific ITCZ forms a band of moist air in all cases, but varies in width and latitudinal location in a case dependent manner as it extends to the east of the date line. Another notable feature in Fig. 1 is that the areas of heavy precipitation, marked by reddish colors, are occasionally confined to along the edge of ITCZ rather than at the heart


of it. Edge intensification events are found on the northern edge of the ITCZ in some cases (160°–140°W on 14 July 2006 and 130°–115°W on 1 September 2008) and on the southern edge in others (155°–140°W on 17 December 2006 and 110°–95°W on 27 June 2009). The edge intensification of convection may be counterintuitive in that the ITCZ is exposed to dry subtropical air at the edges, where convection is more likely to be suppressed than invigorated (e.g., Neggers et al. 2007). The cases presented here were chosen subjectively from the daily snapshots including edge intensification events, but in fact similar events are not rare as will be shown later in section 2b.

The edge intensification of ITCZ convection has not been well documented in the literature. A careful survey of radiative–convective equilibrium (RCE) simulations, nonetheless, reveals that convection can intensify near the edge of convective envelopes (Windmiller and Hohenegger 2019, see also their introduction for review). An enhancement of convective activity is sometimes found along the margins of the moist tropics from satellite observations (Mapes et al. 2018). Windmiller and Hohenegger (2019) argued that the edge intensification in idealized RCE simulations arises from a collective effect of consecutively forming cold pools. This study explores the mechanism behind the edge intensification of ITCZ convection in the eastern Pacific.

## 2. Data and method

### a. Data

The present analysis is based on A-Train satellite observations and reanalysis data. The A-Train constellation comprises a suite of satellites flying in formation including *Aqua*, *CloudSat*, and *CALIPSO*. Column water vapor (CWV), surface precipitation, sea surface temperature (SST), and near-surface wind at 10-m height (U10) are obtained from the *Aqua* AMSR-E daily

 Denotes content that is immediately available upon publication as open access.

Corresponding author: Hiro Masunaga, masunaga@nagoya-u.jp

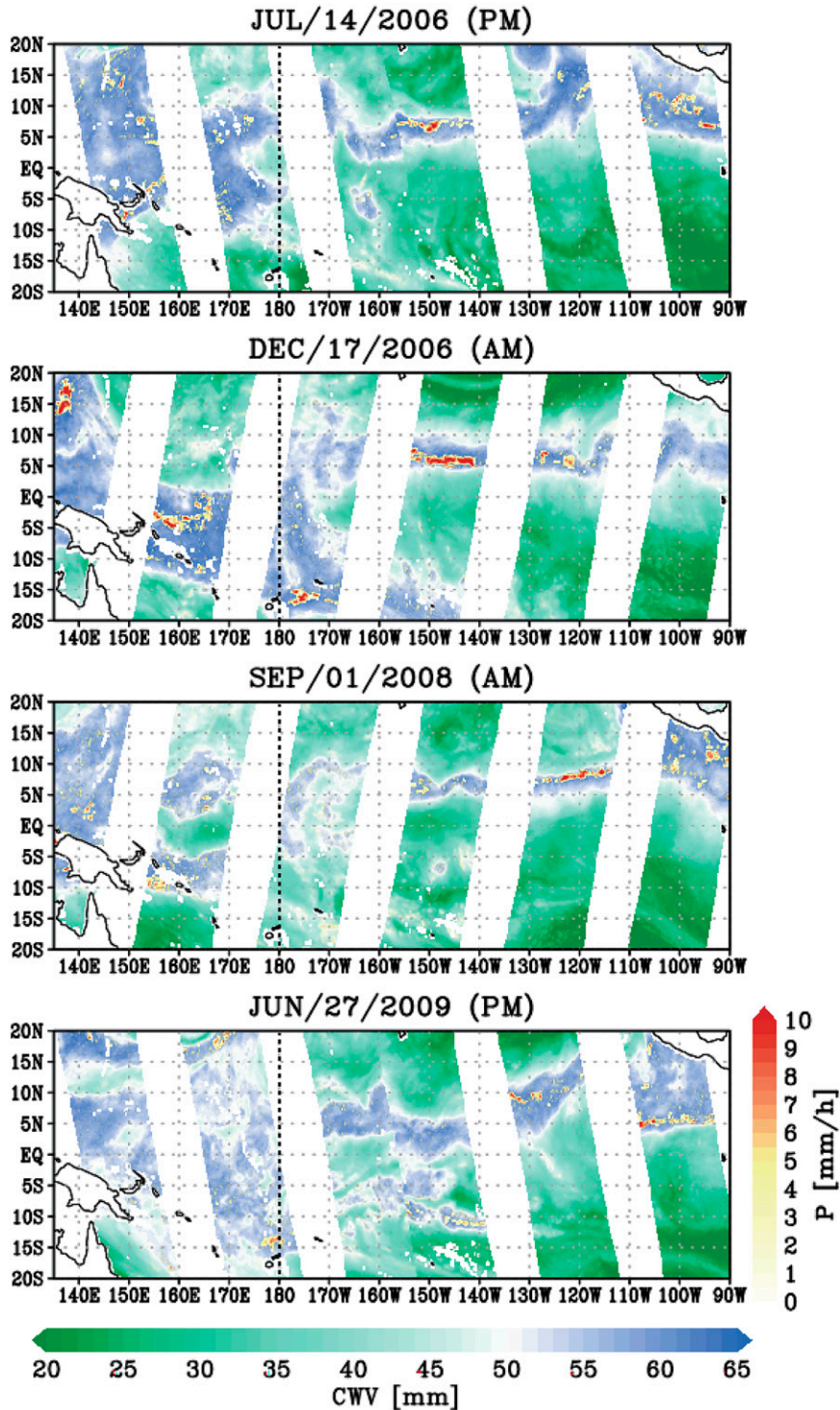


FIG. 1. AMSR-E snapshots of CWV (green-to-blue shading) overlaid by surface precipitation (yellow-to-red shading) over the eastern Pacific for selected dates. PM and AM in the title of each panel refers to the ascending (1330 local time) and descending (0130 local time) tracks, respectively. The date line is marked by a thick dotted line for reference.

data products produced by Remote Sensing Systems (RSS) (Wentz 2013; Hilburn and Wentz 2008). Latent heat flux (LHF) from sea surface is evaluated from SST and U10 using the bulk equation (Large et al. 1994), combined with an empirical formula determining the near-surface water vapor mixing ratio as a function of CWV and SST (see the appendix of Masunaga and L'Ecuyer 2010). The CWV, SST, and U10 estimates are unavailable in heavily raining areas and are each interpolated from neighboring measurements wherever missing due to precipitation. Microwave measurements of SST and U10 tend to be missing in the ocean surfaces covered by significant rainfall, while CWV is affected only by extreme cases. As a result, LHF may rely to a certain extent on the interpolated field around the precipitation peak, but CWV does so only to a very minor degree. The column radiative heating is obtained from the net radiative fluxes at the top and bottom of the atmosphere provided by the *Aqua* CERES Level-2 Single Scanner Footprint (SSF) Edition 4A dataset (Su et al. 2015). The vertical structure of cloud radiative effect (CRE) is provided by the *CALIPSO*, *CloudSat*, CERES, and MODIS (CCCM) Release D1 product (Kato et al. 2011).

The vertical profiles of air temperature ( $T$ ), water vapor mixing ratio ( $q_v$ ), horizontal wind ( $u$  and  $v$ ), and vertical pressure velocity ( $\omega$ ) are taken from the ERA5 data (Hersbach et al. 2020). The ERA5 variables, originally stored as hourly time series, are interpolated over time to the 0130 and 1330 local time A-Train ground tracks from the two temporal neighbors. All the satellite and ERA5 data are matched together on a  $0.25^\circ$  grid where AMSR-E and CERES data are both available. As an exception, the CCCM composite plots are constructed separately with nadir tracks only.

The data period spans 4.5 years from 1 July 2006 to 31 December 2010. The target region is the tropical eastern Pacific as defined by  $20^\circ\text{S}$ – $20^\circ\text{N}$ ,  $180^\circ$ – $90^\circ\text{W}$  with islands excluded. The portion of the Isthmus of Panama and the Caribbean Sea that falls in this domain is also discarded from the analysis. The ERA5 air temperature is averaged at each pressure level over the same period and region as above to obtain the climatological stability profile required for the vertical normal mode transform.

### b. Compositing method

A composite analysis is carried out to explore the statistical characteristics of the edge intensification. The methodology is described below.

Different ways have been proposed to objectively identify the ITCZ from observations (e.g., Wodzicki and Rapp 2016, and references therein). The current study adopts a new, simple approach based on a fixed CWV threshold of 50 mm. This particular value was inspired by the 48-mm margin separating the moist tropics from the dry subtropics (Mapes et al. 2018), which has a physical basis in that a CWV of 48 mm roughly corresponds to the neutrality in the atmospheric energy budget (Masunaga and Mapes 2020). The ITCZ is required to be moister than 50 mm, visualized as blue-colored areas to contrast with the surrounding, green-colored regions in Fig. 1.

Sequences of A-Train measurements are sampled in the direction parallel to the subsatellite track across the full width

of the 1450-km-wide AMSR-E swath, with the exception of the nadir-only CCCM measurements. Since the *Aqua* satellite is a polar orbiter with an orbital inclination of about  $98^\circ$ , each sampled sequence follows a quasi-north–south path. The ITCZ is defined by the along-track segments where CWV continuously exceeds 50 mm. The southern (northern) edge of the ITCZ is the point where CWV increases northward (southward) across 50 mm, with the midpoint between the southern and northern edges being the ITCZ center. In case where multiple bands of ITCZ are identified along the same satellite track, they are treated as individual samples, whether they are genuinely separate (e.g., double ITCZs) or different portions of the same meandering system.

A composite ITCZ is constructed by averaging a large number of the ITCZ segments together. Composite statistics are broken down into three categories depending on where the precipitation maximum is located. If the ITCZ precipitation maximum is found within 100 km from the southern edge of the ITCZ, the observations are stored for the *south-edge* composite category. Similarly, the *north-edge* category is defined with the precipitation peaks detected within 100 km from the northern ITCZ edge. As a reference, the *center-peaked* composite is constructed when the precipitation maximum falls within  $\pm 50$  km about the ITCZ center. As such, all the three cases share the same search radius of 100 km, ensuring that the likelihood of ITCZ occurrence is not artificially skewed among the cases. Changing the 100-km margin or the 50-mm threshold to a larger value would push the “edge” deeper into the ITCZ, blurring the distinction between the edge and center-peaked composites. It is reiterated that the 50-mm threshold is intended as a physically based measure of the ITCZ that the net input of thermal energy to the atmosphere via radiation and surface heat fluxes is positive inside the ITCZ while negative outside (Masunaga and Mapes 2020).

The south-edge, north-edge, and center-peaked composite groups are each partitioned further into subcategories divided by different ITCZ widths of 300–400, 400–600, 600–800, and 800–1000 km. ITCZ samples narrower than 300 km are discarded from the analysis because otherwise there would be edge-intensification cases that cannot be unambiguously separable from the center-peaked case.

Figure 2 shows the number of detected ITCZ events that constitute each composite category. It is noted that an “ITCZ event” is meant to be each ITCZ segment sampled by a single satellite track. The satellite tracks are projected on a  $0.25^\circ$  global grid in the current analysis, so that a group of neighboring  $0.25^\circ$ -wide satellite tracks parallel to one another constitute each satellite swath as shown in Fig. 1. As such, a single band of ITCZ precipitation is counted more than once if intersected multiple times by adjacent satellite tracks, so that an elongated ITCZ feature is weighted more than a shorter one in the histogram. As may be expected, center-peaked composite events are observed more often than each of south- and north-edge events for all ITCZ widths. The edge-intensification cases are, nevertheless, far from rare in that a precipitation peak occurs near the southern or northern edge of the ITCZ roughly or more than half as frequently as at the ITCZ center.

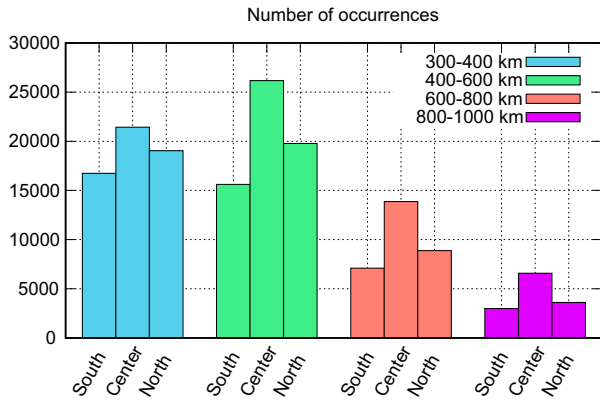


FIG. 2. Histogram of ITCZ events for different ITCZ widths as indicated by legend. “South,” “north,” and “center” on the abscissa refer to the south-edge, north-edge, and center-peaked cases, respectively. See text for the precise definition of “ITCZ events.”

3. Results

a. Precipitation and moisture convergence

The precipitation distribution across the ITCZ for different composite categories is plotted in Fig. 3. The abscissa is the distance along the A-Train ground tracks (northward positive) relative to the ITCZ midpoint in the center-peaked case and to the corresponding ITCZ edge in the south- and north-edge cases. Composite precipitation by construction rises to a

maximum exactly at distance zero in center-peaked cases, with the peak height increasing with the ITCZ width. The south-edge (north-edge) composite precipitation has a peak slightly shifted northward (southward) from the edge. It follows that the edge intensification of convection occurs on the moist side of the 50-mm boundary of the ITCZ. The composite precipitation peak is weaker when occurring at the ITCZ edges than at the ITCZ center.

To verify the validity of using a fixed CWV threshold to define the ITCZ, column-integrated moisture convergence is examined in composite space (Fig. 4). The center-peaked composite curve in Fig. 4a (300–400-km width) implies that moisture convergence stays positive over a distance of  $\pm 200$  km about the ITCZ midpoint. In the edge intensification cases of Fig. 4a, moisture convergence is positive over a width of  $\sim 400$  km with its peak shifted to the negative (southern) side for the north-edge composite and to the positive (north) side for the south-edge composite. This confirms that a moist band identified by the 50-mm threshold overall agrees with an independent (and more authentic) definition of the ITCZ based on moisture convergence. It is noted that the CWV threshold has been adopted instead of moisture convergence for the event-by-event detection of the ITCZ because the moisture convergence field is rather noisy on an instantaneous basis.

Figures 4b–d shows the same plots but for different widths of 400–600, 600–800, and 800–1000 km. The span of positive moisture convergence increases roughly in accordance with increasing ITCZ width, although apt to be near (or slightly

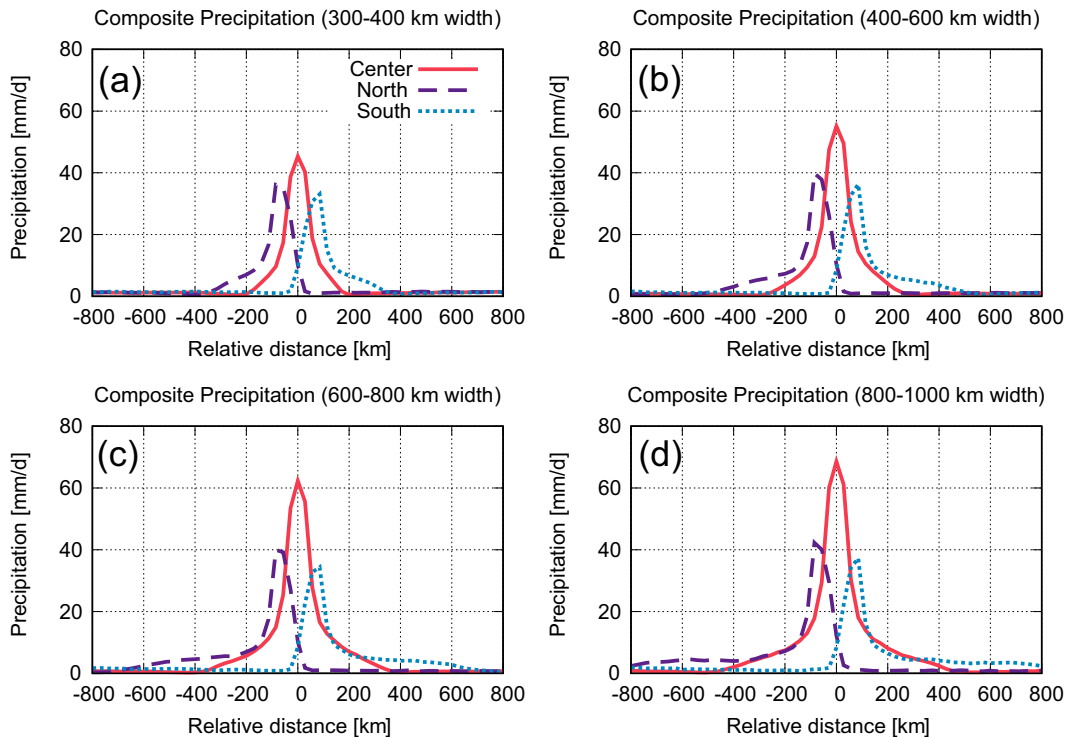


FIG. 3. Composite precipitation for different ITCZ widths of (a) 300–400, (b) 400–600, (c) 600–800, and (d) 800–1000 km. The center-peaked, north-edge, and south-edge cases are shown in solid, dashed, and dotted curves, respectively. See text for the definition of the relative distance (abscissa).

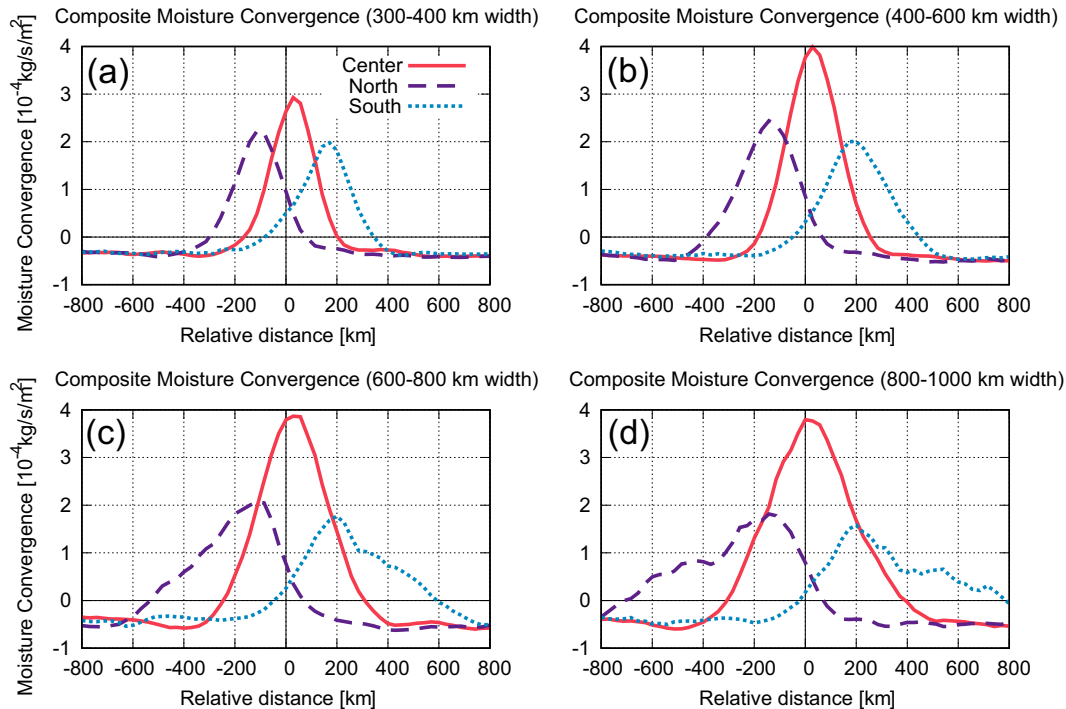


FIG. 4. As in Fig. 3, but for moisture convergence integrated over height.

short of) the lower end of each range (e.g.,  $\sim 800$  km for the case of 800–1000 km).

It is shown in Figs. 3 and 4 that the ITCZ is approximately “scale-free” in that the horizontal structure of precipitation and moisture convergence is qualitatively similar regardless of the ITCZ width. Only the composite category of 400–600 km, having the largest sample size and hence statistically most robust (Fig. 3), will be discussed in the remainder of this paper except where otherwise noted. Results for other ITCZ widths do not alter any main conclusion of the current paper.

#### b. MSE budget breakdown

A moist static energy (MSE) budget analysis is carried out in composite space for illustrating the key processes at work behind the edge intensification of ITCZ convection. MSE per unit mass, defined as  $c_p T + \phi + Lq_v$ , where  $c_p$  is the specific heat of air at constant pressure,  $\phi$  is geopotential, and  $L$  is the specific latent heat of vaporization, is conserved in moist adiabatic processes in a hydrostatic atmosphere, and therefore is a useful measure of large-scale convective dynamics. The evolution of vertically integrated MSE satisfies the MSE budget equation:

$$\langle \partial_t h \rangle + \langle \mathbf{u} \cdot \nabla h \rangle + \langle \omega \partial_p h \rangle = F_L + F_S + \langle Q_R \rangle, \quad (1)$$

where  $\mathbf{u}$  is horizontal wind,  $F_L$  is LHF,  $F_S$  is sensible heat flux (SHF),  $Q_R$  is radiative heating rate, and  $\langle \dots \rangle$  denotes the vertical integral over the whole thickness of the atmosphere. For ease of reference, the MSE budget terms are hereafter denoted as

$$\langle \partial_t h \rangle = \text{HADV} + \text{VADV} + \text{NDF}, \quad (2)$$

where HADV, VADV, and NDF refer to the vertically integrated horizontal advection of MSE, the vertically integrated vertical advection of MSE, and the net diabatic forcing, respectively:

$$\text{HADV} \equiv -\langle \mathbf{u} \cdot \nabla h \rangle,$$

$$\text{VADV} \equiv -\langle \omega \partial_p h \rangle,$$

$$\text{NDF} \equiv F_L + F_S + \langle Q_R \rangle.$$

As described above in section 2a,  $F_L$  and  $\langle Q_R \rangle$  are estimated from satellite measurements while  $h$ , HADV, and VADV are derived from the ERA5 datasets matched in space and time with A-Train observations. SHF stays small in magnitude compared to LHF and column radiative heating over tropical oceans, so  $F_S$  is fixed at a typical value of  $10 \text{ W m}^{-2}$  in the current analysis.

The three terms on the rhs of (2) each have essential roles in tropical dynamics. NDF collectively represents the rate of thermal energy input to (or, if negative, output from) the atmosphere, acting as the “external” forcing that drives the atmospheric circulation. Here NDF is referred to as external in that NDF has no explicit reference to the large-scale meteorological state ( $T$ ,  $q_v$ ,  $\mathbf{u}$ , and  $\omega$ ), but is likely to be implicitly intertwined with these variables through various processes such as the anvil cloud effects on  $\langle Q_R \rangle$ .

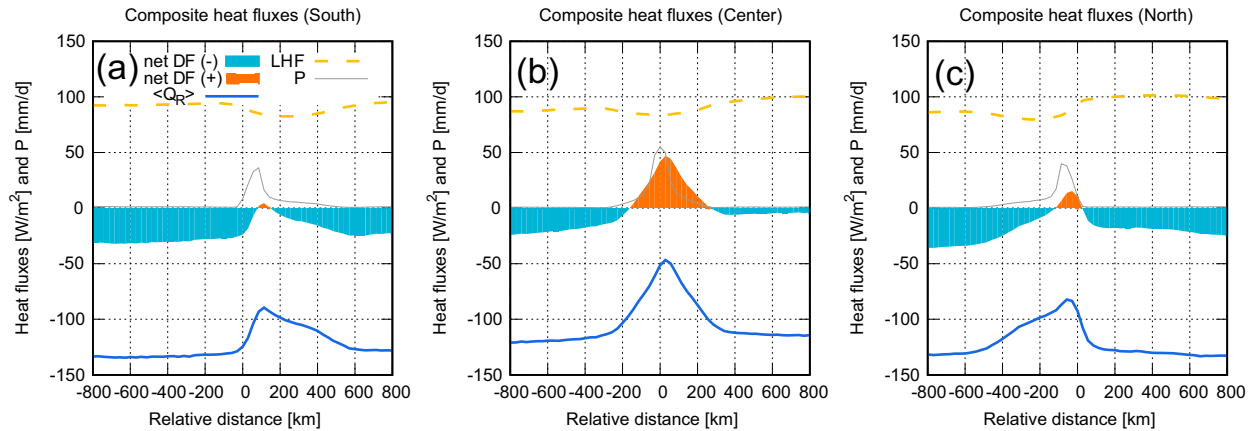


FIG. 5. Diabatic forcing terms ( $\text{W m}^{-2}$ ) in composite space, that is, column radiative heating ( $\langle Q_R \rangle$ ) (solid), LHF  $F_L$  (dashed), and the NDF or  $F_L + F_S + \langle Q_R \rangle$  (shaded) for (a) south-edge, (b) center-peaked, and (c) north-edge composites. Precipitation ( $\text{mm day}^{-1}$ ) is shown as a thin curve for reference.

VADV, quantifying the import (export) of MSE into (from) an atmospheric column owing to the internal dynamics within the column, is a variable sensitive to the depth of circulation and hence to details in the moist convective processes as will be demonstrated later. Changes in the column-integrated MSE due to the large-scale horizontal transport are summarized by HADV. Since free-tropospheric temperature is nearly horizontally uniform in the low-latitude atmosphere, HADV is primarily governed by the horizontal gradient of moisture and the horizontal wind field.

### c. Diabatic forcing

The composite spatial structure of NDF is first investigated. Figure 5 shows the composite spatial structure of column radiative heating (solid), LHF (dashed), and NDF. LHF is largely counteracted by column radiative cooling (i.e., negative  $\langle Q_R \rangle$ ), leading to a weakly negative NDF except near distance zero. In the center-peaked composite (Fig. 5b), NDF has a distinct maximum of  $+50 \text{ W m}^{-2}$  around the precipitation peak at the ITCZ center, tapering off nearly symmetrically on both sides to a negative value at distances beyond  $\pm 200 \text{ km}$ . This spatial

variability in the diabatic forcing arises principally from that of column radiative heating, while LHF has little horizontal variability.

NDF reaches a maximum roughly in phase with the precipitation peak in the edge intensification cases as well (Figs. 5a,c), whereas the peak height is only barely positive. The spatial variation of  $\langle Q_R \rangle$  is asymmetric about the peak, accompanied by a more gradually decreasing shoulder to inside the ITCZ than to outside.

The spatial structure of column radiative heating is mainly accounted for by the anvil cloud effects as illustrated by the vertical profile of the net CRE (Fig. 6). The net CRE is enhanced in the upper troposphere (8–13 km in height), which is a combined effect of shortwave and longwave heating by anvil clouds. The horizontal distribution is approximately symmetric in the center-peaked case (Fig. 6b) while asymmetric in the south- and north-edge cases (Figs. 6a,c) just as seen in column radiative heating (Fig. 5). The anvil cloud heating is partially offset to a minor extent by a negative CRE observed at altitudes of 13–15 km, attributable to the cloud-top longwave cooling associated with deep convection. A narrow layer of

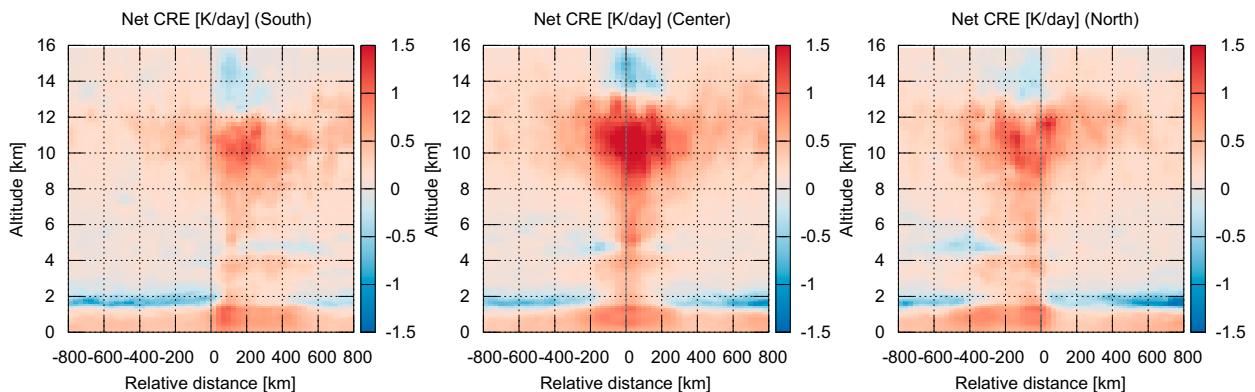


FIG. 6. The vertical structure of the net CRE ( $\text{K day}^{-1}$ ) in composite space for (a) south-edge, (b) center-peaked, and (c) north-edge composites.

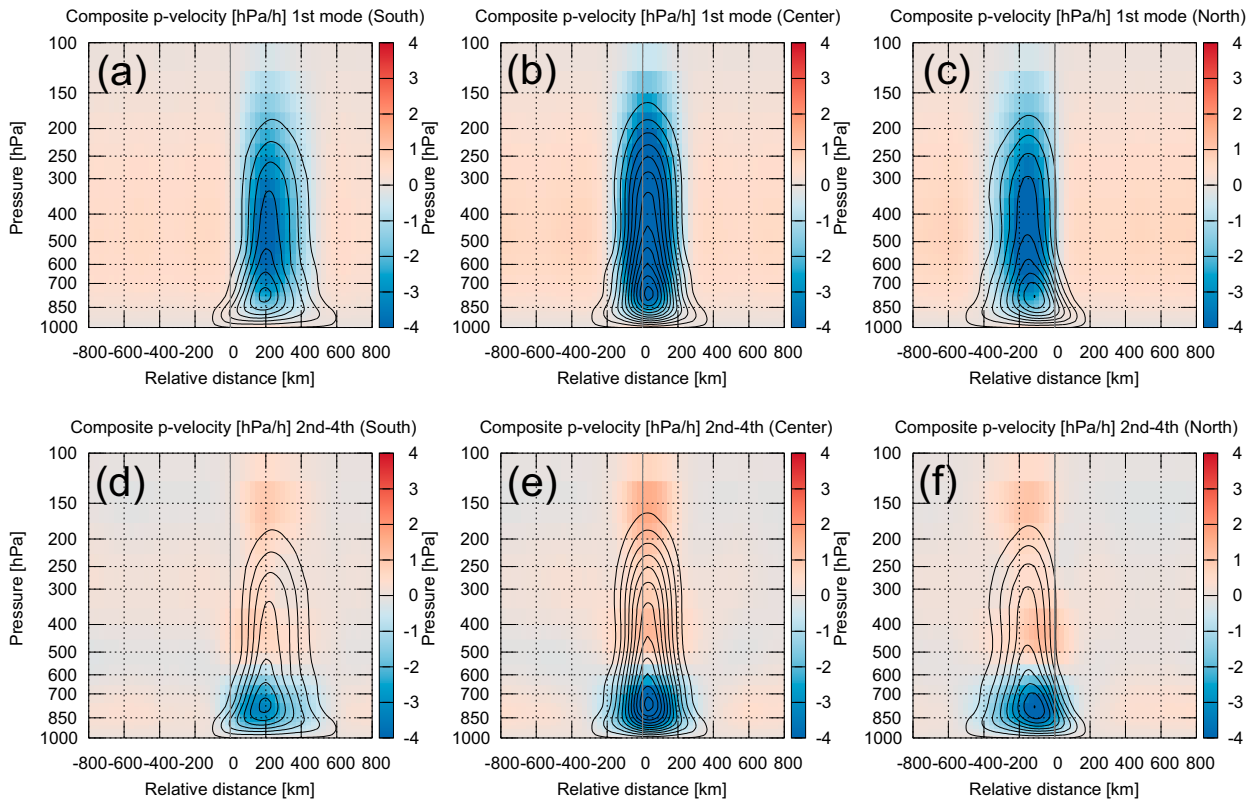


FIG. 7. The vertical structure of  $\omega$  ( $\text{hPa h}^{-1}$ ) and its vertical mode decomposition in composite space for (a) south-edge, (b) center-peaked, and (c) north-edge composites. The deep mode or the first mode is shaded in color and the original (undecomposed)  $\omega$  profile is contoured at an interval of  $1 \text{ hPa h}^{-1}$  for ascent (negative  $\omega$ ) only. (d)–(f) As in (a)–(c), but for the shallow mode or the second to fourth modes summed together (color).

longwave cooling at shallow cloud tops is visible at a height of 2 km, which would be largely canceled out by a layer of cloud longwave heating immediately below when integrated vertically into  $\langle Q_R \rangle$ .

#### d. Vertical mode decomposition

VADV can change not only in amplitude but in sign depending on the vertical structure of  $\omega$ . Given a typical vertical profile of MSE over tropical oceans, a top-heavy  $\omega$  profile exports MSE out of the atmospheric column while a bottom-heavy one could import MSE into the column (e.g., Back and Bretherton 2006; Raymond et al. 2009; Inoue and Back 2015). To quantify the bottom-heaviness, a vertical mode decomposition is applied to the ERA5  $\omega$  profiles. The mode decomposition is carried out by the vertical normal mode transform based on the eigenvalue solution to the vertical component of the linearized primitive equations (Fulton and Schubert 1985; Haertel and Johnson 1998).

The results of vertical mode decomposition are presented in Fig. 7. Ascent motion is concentrated around the center as revealed by the  $\omega$  profiles (contoured). The area of ascent is somewhat displaced to the north in the south-edge case and to the south in the north-edge case, which is in line with the precipitation peak (Fig. 3). The  $\omega$  profiles are consistently bottom-heavy with its peak located at a level near 800 hPa. The top row of Fig. 7 shows the first normal mode in color, accounting for the

deep component of the ascent extending throughout the troposphere. On the other hand, the sum of the second to fourth modes as colored in the bottom row is comprised of a lower-tropospheric ascent, characterizing the bottom-heavy component. The first mode is hereafter called the *deep mode* and the second to the fourth modes in combination are referred to as the *shallow mode*. The individual effects of the deep and shallow modes on VADV are assessed in the subsequent subsection.

#### e. Vertical and horizontal advectations of MSE

VADV is expanded into a series of normal modes:

$$\text{VADV} = \text{VADV}_d + \text{VADV}_s + \text{VADV}_r,$$

with

$$\text{VADV}_d = -\langle \omega_1 \partial_p h \rangle,$$

$$\text{VADV}_s = -\sum_{i=2}^4 \langle \omega_i \partial_p h \rangle,$$

$$\text{VADV}_r = -\sum_{i=5}^{\infty} \langle \omega_i \partial_p h \rangle,$$

where  $\omega_i$  refers to the  $i$ th normal mode and the subscripts  $d$ ,  $s$ , and  $r$  denote the deep mode, shallow mode, and residual,

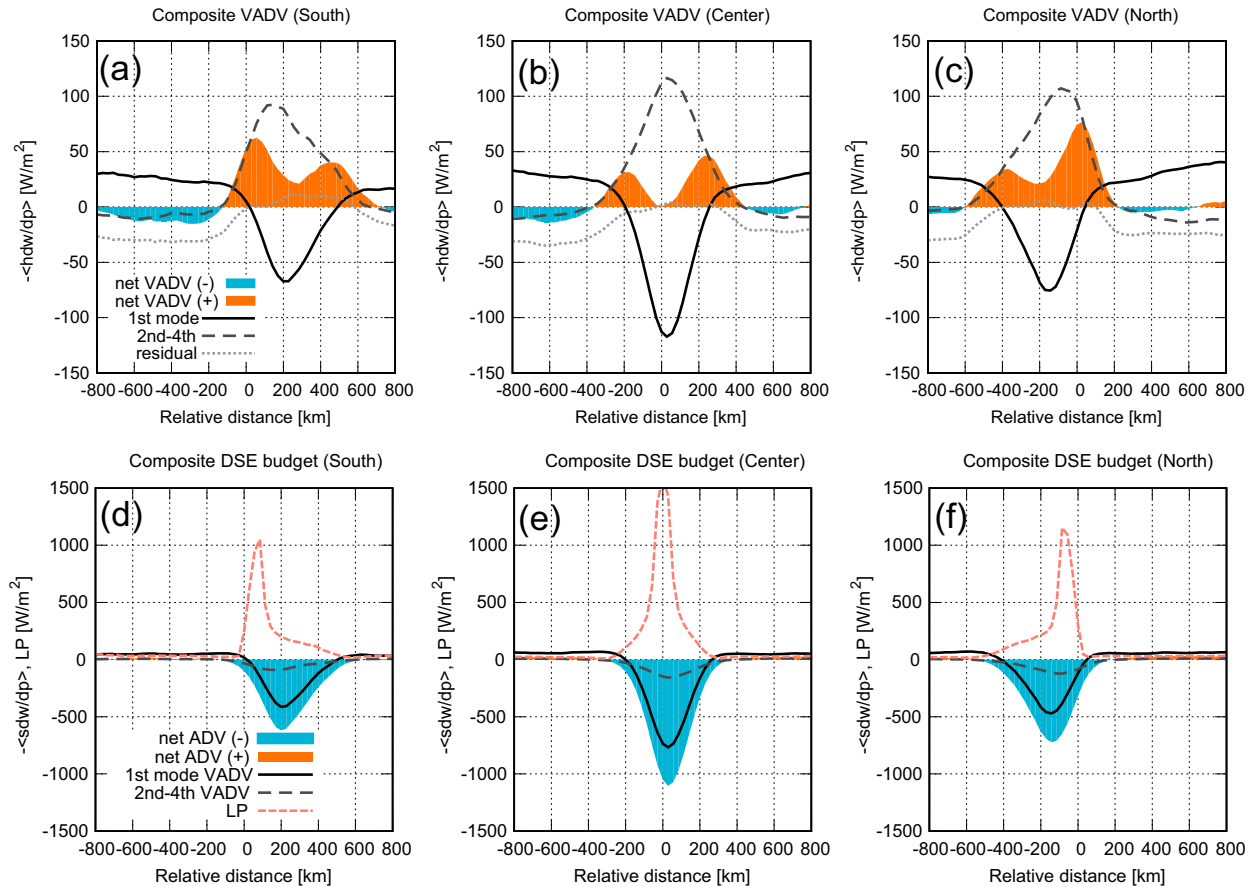


FIG. 8. (a)–(c) Column-integrated vertical MSE advection or VADV ( $W m^{-2}$ ; shaded) and its vertical mode decomposition (solid curve for VADV<sub>d</sub>, dashed for VADV<sub>s</sub>, and dotted for VADV<sub>r</sub>) for (a) south-edge, (b) center-peaked, and (c) north-edge composites. (d)–(f) As in (a)–(c), but for column-integrated net DSE advection (shaded), the vertical mode decomposition of vertical DSE advection (black solid and dashed curves), and precipitation in the units of  $W m^{-2}$  (orange dashed curve). Note that the sign of the advection terms is defined to be positive (negative) for an import (export) of MSE and of DSE.

respectively. Figures 8a–c shows the vertical mode decomposition of VADV. In the area of ascent near distance zero, VADV<sub>d</sub> exhibits a striking negative peak, implying that MSE is exported in the upper troposphere to a greater extent than imported near the surface by a deep overturning circulation represented by the deep mode. In contrast, a shallow ascent associated with VADV<sub>s</sub> results in a net import of MSE, accounting for the positive peak of VADV<sub>s</sub>. VADV<sub>d</sub> and VADV<sub>s</sub> almost precisely cancel each other out at distance zero in the center-peaked case, while the deep mode is not so intense as to entirely counteract the shallow mode in the edge intensification cases. The residual term stays close to zero where VADV<sub>d</sub> and VADV<sub>s</sub> are each enhanced in magnitude, suggesting that the deep and shallow modes well account for the large-scale dynamics inside the ITCZ. The residual is not negligible in the areas of subsidence outside the ITCZ.

For comparison, the leading terms of dry static energy (DSE, defined by  $c_p T + \phi$ ) budget are plotted in Figs. 8d–f. The net DSE advection, practically identical to its vertical component since the horizontal component is negligibly small, is nearly a mirror image of precipitation but with the opposite sign. This

confirms that the condensation heating (or precipitation) is largely counteracted by vertical DSE advection or the adiabatic cooling due to large-scale ascent, primarily accounted for by the deep (first baroclinic) mode. The precipitation peak is somewhat sharper than the corresponding peak of DSE advection. It is unclear whether this discrepancy is a real signal or due to an artifact in the reanalysis data.

Figures 9a–c shows HADV with its zonal and meridional breakdowns. HADV has a large negative value in the right half of the south-edge composite plot (Fig. 9a), in the left half of the north-edge composite (Fig. 9c), and symmetrically about distance zero in the center-peaked case (Fig. 9b). As such, horizontal winds export MSE out of the atmospheric column deep inside the ITCZ, while the export of MSE rapidly decays outward across the ITCZ edge. This behavior of HADV is ascribed principally to the meridional component, with the contribution of the zonal advection being secondary.

To understand the origins of meridional MSE advection, the vertical structures of meridional wind ( $v$ ) and the meridional gradient of MSE ( $\partial_y h$ ) are plotted in Figs. 9d–f. It is noted that the composite means of  $v$  and  $\partial_y h$  are not directly combined



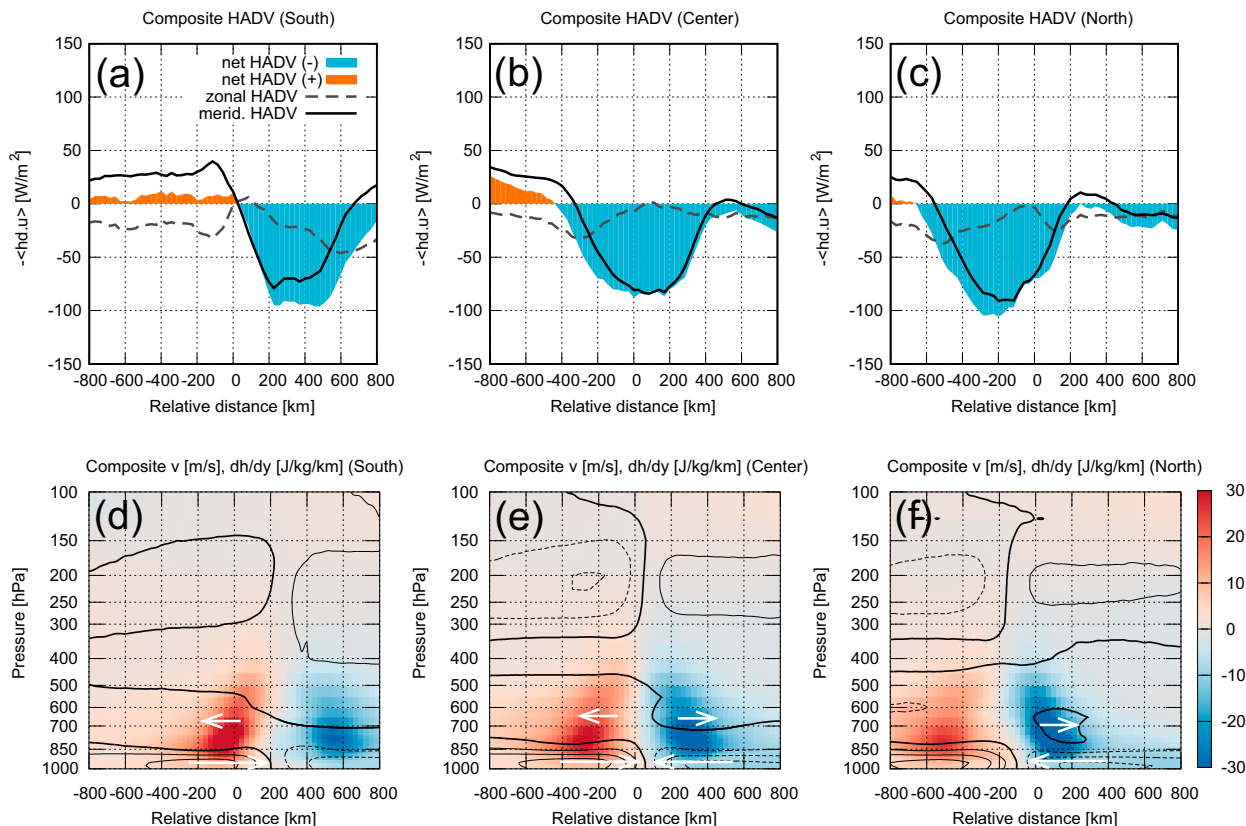


FIG. 9. (top) Column-integrated horizontal MSE advection or HADV ( $\text{W m}^{-2}$ ; shaded) along with its zonal (dashed curve) and meridional (solid curve) components for (a) south-edge, (b) center-peaked, and (c) north-edge composites. (bottom) Vertical structure of  $\partial_y h$  (shaded) and meridional wind (contoured) for (d) south-edge, (e) center-peaked, and (f) north-edge composites. The contour interval is  $1 \text{ m s}^{-1}$  with negative (northerly) contours dashed and zero contours thickened. White arrows indicate the meridional wind direction.

into the mean meridional advection because of nonlinearity ( $\overline{v\partial_y h} \neq \overline{v}\partial_y h$ ) but are nonetheless beneficial for an intuitive illustration. For the center-peaked composite (Fig. 9e), boundary layer inflows from both north and south converge at the ITCZ center. Since the lower tropospheric air is substantially drier outside the ITCZ than in the ITCZ center, the inward transport of the boundary layer MSE is guaranteed to reduce MSE in the ITCZ, accounting for the negative HADV deep inside the ITCZ. On the other hand, a weak return flow immediately above the boundary layer, signifying a shallow meridional circulation typical of the eastern Pacific ITCZ (Zhang et al. 2004), has the effect of moistening the ITCZ edges by carrying the midlevel humid air from the ITCZ center. This midlevel moistening effect is efficient, as implied by the prominent meridional gradient of MSE (shaded) on both sides of the ITCZ, in offsetting the low-level drying when integrated over height. As a result, HADV rapidly diminishes in magnitude from the ITCZ center toward the edges. A close inspection of Fig. 9 reveals that the HADV variability is not precisely symmetric between the south- and north-edge cases: the net HADV almost vanishes or is slightly positive at negative distances in the south-edge composite (Fig. 9a), while HADV stays negative entirely in the north-edge composite (Fig. 9c). This asymmetry leads to discernible consequences on the total MSE advection as discussed later.

The net effect of column-integrated MSE advection (VADV + HADV) is shown in Fig. 10. A confined peak of the net MSE advection stands out at distance zero, flanked by valleys of a near-zero or negative MSE on both sides for the south-edge composite (Fig. 10a). The peak is attributed to VADV, while the valleys result from a competing effect between VADV and HADV being opposite in sign. In contrast, the center-peaked composite plot gives no hint of a positive peak (Fig. 10b), for which the double-peaked MSE import by VADV is more than offset by the significant export of MSE by horizontal advection and hence HADV practically dominates the net MSE advection. The north-edge composite (Fig. 10c) resembles the south-edge case, although the peak is much weaker. This muted magnitude of advection peak in the north-edge case is ascribed to a negative HADV that works against the VADV peak, which would otherwise give rise to a peak of comparable strength to the south-edge composite. VADV is more or less symmetric between the north- and south-edge cases, while HADV is less so as noted earlier.

The composite plots shown in Figs. 5–9 are constructed for the ITCZs having moderate widths of 400–600 km. For comparison, the composite VADV and HADV for broader ITCZs of 600–800 km are plotted in Figs. 10d–f. The peak of the net MSE advection in the north-edge composite is

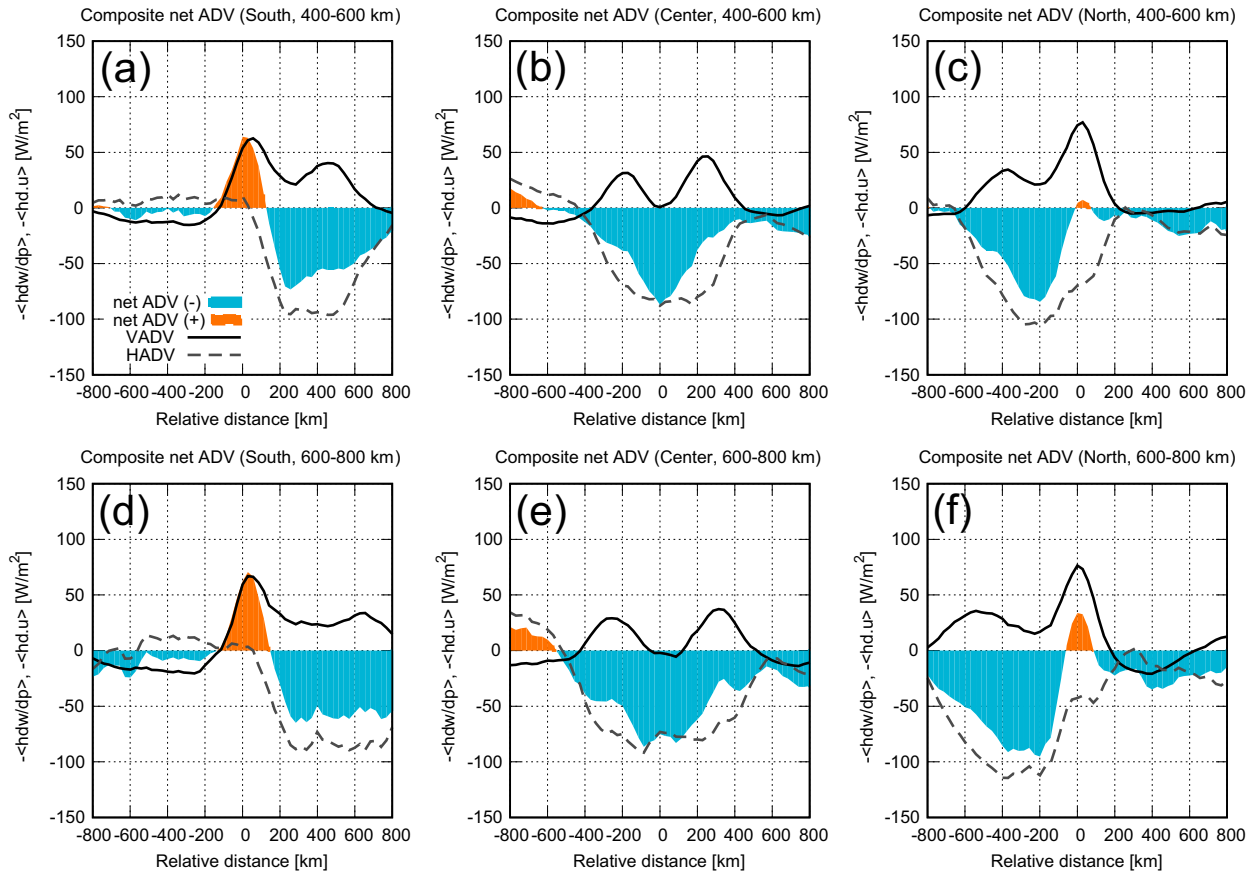


FIG. 10. Column-integrated net MSE advection (VADV + HADV) ( $W m^{-2}$ ; shaded) along with VADV (solid curve) and HADV (dashed curve) for (a) south-edge, (b) center-peaked, and (c) north-edge composites. (d)–(f) As in (a)–(c), but for broader ITCZs (600–800 km) instead of 400–600 km.

more salient for broad ITCZs (Fig. 10f) than for modest ITCZ widths (Fig. 10c), but otherwise there is no qualitative difference.

The key finding here is that the column-integrated net MSE advection exhibits contrasting behaviors between the edge and center intensification cases. The vertical advection of MSE gives rise to an import of MSE sharply confined near the precipitation peak in the edge intensification cases, whereas the precipitation peak is accompanied by an export of MSE when occurring at the ITCZ center. This fundamental difference, along with the contrast in NDF as discussed earlier, suggests that an edge intensification is likely driven by a mechanism distinctly different from the one governing the convective intensification at the heart of the ITCZ.

#### 4. Conclusions and discussion

This study explores the possible mechanism of ITCZ convection with focus on the edge intensification cases. Observations from a suite of A-Train satellite instruments were employed to identify the ITCZ as a band of moist air with CWVs greater than 50 mm. The internal structure of the ITCZ sampled along satellite tracks is averaged together into

a composite diagram around the ITCZ edge or the center, separated by ITCZ width (400–600 and 600–800 km, etc.) and the location of precipitation maximum (south-edge, center-peaked, and north-edge). The edge intensification cases are not as frequent as the typical case where convection is most active in the middle of the ITCZ, but nonetheless are far from rare.

The MSE budget terms were projected onto composite space to reveal the behavior of NDF to the atmosphere and the MSE advection (VADV and HADV). When convection peaks at the ITCZ center, column radiative cooling is strongly suppressed owing to the extensive anvil clouds accompanying deep convection, forming a prominent positive peak in NDF. The total MSE advection in this case is negative as the combined effects of a strong deep-mode VADV and the transport of dry air from outside the ITCZ, both resulting in an export of MSE. When convection peaks at the ITCZ edges, in contrast, a positive peak of NDF is present but substantially weaker than in the center-peaked case. Instead, shallow-mode VADV leads to a net import of MSE on the ITCZ edges, which presumably allows an edge intensification to occur despite the weak NDF. The shallow-mode VADV plays a key role in both the south- and north-edge cases, while the

net advection peak is weaker in the north-edge composite because HADV differs in magnitude between the two cases.

Shallow convection has been known to be instrumental for promoting a subsequent development of deeper convection. The deepening of shallow cumulus clouds to deep convection is often observed in association with a low-level accumulation of moisture in the growing phase of the MJO (Lin and Johnson 1996a,b; Kemball-Cook and Weare 2001). Such a “pre-conditioning” effect has been argued in the literature to occur through a variety of processes including the detrainment of moisture from congestus clouds (Takayabu et al. 2006; Waite and Khouider 2010) and large-scale moisture convergence (Hohenegger and Stevens 2013; Masunaga 2013). A shallow overturning (or bottom-heavy) circulation coupled with moist processes has the potential of dynamically amplifying itself under a negative gross moist stability (GMS), marking a sharp contrast to deep (top-heavy) convection, which has a positive GMS and is self-destructive by nature (Back and Bretherton 2006; Raymond et al. 2009; Back and Bretherton 2009; Masunaga and L’Ecuyer 2014; Inoue and Back 2015). Inoue et al. (2021) showed that convective dynamics is maintained over tropical oceans through regionally dependent feedback processes: a negative GMS due to shallow circulation is a primary driver of convection in some regions while a feedback involving the interplay of NDF with deep convection plays a major role in others. The current analysis implies that such different processes could coexist within the eastern Pacific ITCZ, with the diabatic feedback being at work in its center and a negative GMS driving convection at the edges.

Other processes potentially accounting for the edge intensification of convection include a “super cold pool,” or an ensemble of sequentially generated cold pools pushing convection toward the edge of a convectively active region. The super-cold-pool theory for the edge intensification of convection, elaborated by Windmiller and Hohenegger (2019) based on their numerical simulations, may also contribute to the observed enhancement of convection along the ITCZ edges, although difficult to prove or disprove in the current analysis approach because cold pools, particularly when concealed by overlying clouds, are hard to track from satellite observations and reanalysis data.

It is possible that two contrasting convective events, one at the ITCZ center and the other at the edge, can belong to the same convective system at different stages of the life cycle. The super-cold-pool theory predicts that convection initiated at the center of a moist patch would propagate to the edge as a series of cold pools crawl forward. To the contrary, a Lagrangian air parcel carried along the lower branch of the Hadley cell would first give rise to an edge intensification of convection before eventually arriving in the ITCZ center (Masunaga and Mapes 2020). The evolution from one convective event to another is not easy to explore in the current analysis because of the inability to continuously observe the same event from low-Earth-orbiting satellites but is an interesting subject worth investigating in the future possibly with the aid of geostationary infrared imagery.

The meridional overturning circulation associated with ITCZ convection differs in depth between the edge- and center-intensification cases, potentially imposing different consequences on the atmospheric energy transport (AET). A

shallow circulation as found typically with the edge intensification has a poleward flow in the midtroposphere instead of the upper troposphere, and thus would have a moderate AET compared to the deep Hadley cell, all else being equal, since DSE and MSE are lower in the midtroposphere than at higher levels. It should be noted, however, that edge-intensification events are unlikely to significantly affect the AET on a global scale because an area of enhanced ITCZ convection is so fragmentary on an instantaneous basis (see Fig. 1) that the edge effects would be averaged out in the zonal mean.

The present analysis strategy is in theory equally applicable to global tropical oceans, except that the existence of islands (in the western Pacific Ocean) and of continents to the immediate north or south of the ITCZ (in the Indian and Atlantic Oceans) somewhat challenges the ability to unambiguously detect the ITCZ edges with microwave measurements of CWV. Future work comparing similarities and differences across different regions would potentially offer a more comprehensive insight on the ITCZ dynamics in light of how moist convection is maintained.

*Acknowledgments.* This work is supported by Japan Society for the Promotion of Science (JSPS) Grants-in-Aid for Scientific Research (KAKENHI) 19H01966 and 19H05704. The comments by the anonymous reviewer and Margaret Duffy were helpful in revising the paper.

*Data availability statement.* The RSS AMSR-E data may be downloaded from <https://www.remss.com/missions/amr/>. The CERES SSF Edition 4A data are provided by <https://ceres.larc.nasa.gov/data/#ssf-level-2>. The CCCM Release D1 product is available from [https://asdc.larc.nasa.gov/project/CERES/CER\\_CCCM\\_Aqua-FM3-MODIS-CAL-CS\\_RelD1](https://asdc.larc.nasa.gov/project/CERES/CER_CCCM_Aqua-FM3-MODIS-CAL-CS_RelD1) (NASA/LARC/SD/ASDC 2011). The ERA5 dataset is available at <https://cds.climate.copernicus.eu/cdsapp#!/dataset/reanalysis-era5-pressure-levels> (Hersbach et al. 2018).

## REFERENCES

- Back, L. E., and C. S. Bretherton, 2006: Geographic variability in the export of moist static energy and vertical motion profiles in the tropical Pacific. *Geophys. Res. Lett.*, **33**, L17810, <https://doi.org/10.1029/2006GL026672>.
- , and —, 2009: A simple model of climatological rainfall and vertical motion patterns over the tropical oceans. *J. Climate*, **22**, 6477–6497, <https://doi.org/10.1175/2009JCLI2393.1>.
- Crowe, P. R., 1951: Wind and weather in the equatorial zone. *Trans. Pap. Inst. Br. Geogr.*, **17**, 23–76, <https://doi.org/10.2307/621291>.
- Fulton, S. R., and W. H. Schubert, 1985: Vertical normal mode transforms: Theory and application. *Mon. Wea. Rev.*, **113**, 647–658, [https://doi.org/10.1175/1520-0493\(1985\)113<0647:VNMTA>2.0.CO;2](https://doi.org/10.1175/1520-0493(1985)113<0647:VNMTA>2.0.CO;2).
- Haertel, P. T., and R. H. Johnson, 1998: Two-day disturbances in the equatorial western Pacific. *Quart. J. Roy. Meteor. Soc.*, **124**, 615–636, <https://doi.org/10.1002/qj.49712454611>.
- Hersbach, H., and Coauthors, 2018: ERA5 hourly data on pressure levels from 1940 to present. Copernicus Climate Change

- Service (C3S) Climate Data Store (CDS), accessed 4 April 2023, <https://doi.org/10.24381/cds.bd0915c6>.
- , and Coauthors, 2020: The ERA5 global reanalysis. *Quart. J. Roy. Meteor. Soc.*, **146**, 1999–2049, <https://doi.org/10.1002/qj.3803>.
- Hilburn, K. A., and F. J. Wentz, 2008: Intercalibrated passive microwave rain products from the Unified Microwave Ocean Retrieval Algorithm (UMORA). *J. Appl. Meteor. Climatol.*, **47**, 778–794, <https://doi.org/10.1175/2007JAMC1635.1>.
- Hohenegger, C., and B. Stevens, 2013: Preconditioning deep convection with cumulus congestus. *J. Atmos. Sci.*, **70**, 448–464, <https://doi.org/10.1175/JAS-D-12-089.1>.
- Inoue, K., and L. E. Back, 2015: Gross moist stability assessment during TOGA COARE: Various interpretations of gross moist stability. *J. Atmos. Sci.*, **72**, 4148–4166, <https://doi.org/10.1175/JAS-D-15-0092.1>.
- , M. Biasutti, and A. M. Fridlind, 2021: Evidence that horizontal moisture advection regulates the ubiquitous amplification of rainfall variability over tropical oceans. *J. Atmos. Sci.*, **78**, 529–547, <https://doi.org/10.1175/JAS-D-20-0201.1>.
- Kang, S. M., I. M. Held, D. M. W. Frierson, and M. Zhao, 2008: The response of the ITCZ to extratropical thermal forcing: Idealized slab-ocean experiments with a GCM. *J. Climate*, **21**, 3521–3532, <https://doi.org/10.1175/2007JCLI2146.1>.
- Kato, S., and Coauthors, 2011: Improvements of top-of-atmosphere and surface irradiance computations with CALIPSO-, CloudSat-, and MODIS-derived cloud and aerosol properties. *J. Geophys. Res.*, **116**, D19209, <https://doi.org/10.1029/2011JD016050>.
- Kemball-Cook, S. R., and B. C. Weare, 2001: The onset of convection in the Madden–Julian Oscillation. *J. Climate*, **14**, 780–793, [https://doi.org/10.1175/1520-0442\(2001\)014<0780:TOOCIT>2.0.CO;2](https://doi.org/10.1175/1520-0442(2001)014<0780:TOOCIT>2.0.CO;2).
- Large, W. G., J. C. McWilliams, and S. C. Doney, 1994: Oceanic vertical mixing: A review and a model with a nonlocal boundary layer parameterization. *Rev. Geophys.*, **32**, 363–403, <https://doi.org/10.1029/94RG01872>.
- Li, T., 1997: Air–sea interactions of relevance to the ITCZ: Analysis of coupled instabilities and experiments in a hybrid coupled GCM. *J. Atmos. Sci.*, **54**, 134–147, [https://doi.org/10.1175/1520-0469\(1997\)054<0134:ASIORT>2.0.CO;2](https://doi.org/10.1175/1520-0469(1997)054<0134:ASIORT>2.0.CO;2).
- Lin, X., and R. H. Johnson, 1996a: Heating, moistening, and rainfall over the western Pacific warm pool during TOGA COARE. *J. Atmos. Sci.*, **53**, 3367–3383, [https://doi.org/10.1175/1520-0469\(1996\)053<3367:HMAROT>2.0.CO;2](https://doi.org/10.1175/1520-0469(1996)053<3367:HMAROT>2.0.CO;2).
- , and —, 1996b: Kinematic and thermodynamic characteristics of the flow over the western Pacific warm pool during TOGA COARE. *J. Atmos. Sci.*, **53**, 695–715, [https://doi.org/10.1175/1520-0469\(1996\)053<0695:KATCOT>2.0.CO;2](https://doi.org/10.1175/1520-0469(1996)053<0695:KATCOT>2.0.CO;2).
- Mapes, B. E., E.-S. Chung, W. M. Hannah, H. Masunaga, A. J. Wimmers, and C. S. Velden, 2018: The meandering margin of the meteorological moist tropics. *Geophys. Res. Lett.*, **45**, 1177–1184, <https://doi.org/10.1002/2017GL076440>.
- Masunaga, H., 2013: A satellite study of tropical moist convection and environmental variability: A moisture and thermal budget analysis. *J. Atmos. Sci.*, **70**, 2443–2466, <https://doi.org/10.1175/JAS-D-12-0273.1>.
- , and T. S. L'Ecuyer, 2010: The southeast Pacific warm band and double ITCZ. *J. Climate*, **23**, 1189–1208, <https://doi.org/10.1175/2009JCLI3124.1>.
- , and —, 2011: Equatorial asymmetry of the east Pacific ITCZ: Observational constraints on the underlying processes. *J. Climate*, **24**, 1784–1800, <https://doi.org/10.1175/2010JCLI3854.1>.
- , and —, 2014: A mechanism of tropical convection inferred from observed variability in the moist static energy budget. *J. Atmos. Sci.*, **71**, 3747–3766, <https://doi.org/10.1175/JAS-D-14-0015.1>.
- , and B. E. Mapes, 2020: A mechanism for the maintenance of sharp tropical margins. *J. Atmos. Sci.*, **77**, 1181–1197, <https://doi.org/10.1175/JAS-D-19-0154.1>.
- Mitchell, T. P., and J. M. Wallace, 1992: The annual cycle in equatorial convection and sea surface temperature. *J. Climate*, **5**, 1140–1156, [https://doi.org/10.1175/1520-0442\(1992\)005<1140:TACIEC>2.0.CO;2](https://doi.org/10.1175/1520-0442(1992)005<1140:TACIEC>2.0.CO;2).
- NASA/LARC/SD/ASDC, 2011: CERES A-Train integrated CALIPSO, CloudSat, CERES, and MODIS (CCCM) merged release D1. NASA Langley Atmospheric Science Data Center DAAC, accessed 4 April 2023, [https://doi.org/10.5067/AQUA/CERES/CCCM-FM3-MODIS-CAL-CS\\_L2.RELD1](https://doi.org/10.5067/AQUA/CERES/CCCM-FM3-MODIS-CAL-CS_L2.RELD1).
- Neggers, R. A. J., J. D. Neelin, and B. Stevens, 2007: Impact mechanisms of shallow cumulus convection on tropical climate dynamics. *J. Climate*, **20**, 2623–2642, <https://doi.org/10.1175/JCLI4079.1>.
- Philander, S. G. H., D. Gu, D. Halpern, G. Lambert, N.-C. Lau, T. Li, and R. C. Pacanowski, 1996: Why the ITCZ is mostly north of the equator. *J. Climate*, **9**, 2958–2972, [https://doi.org/10.1175/1520-0442\(1996\)009<2958:WTIMN>2.0.CO;2](https://doi.org/10.1175/1520-0442(1996)009<2958:WTIMN>2.0.CO;2).
- Raymond, D. J., S. L. Sessions, A. H. Sobel, and Ž. Fuchs, 2009: The mechanics of gross moist stability. *J. Adv. Model. Earth Syst.*, **1** (3), <https://doi.org/10.3894/JAMES.2009.1.9>.
- Su, W., J. Corbett, Z. Eitzen, and L. Liang, 2015: Next-generation angular distribution models for top-of-atmosphere radiative flux calculation from CERES instruments: Methodology. *Atmos. Meas. Tech.*, **8**, 611–632, <https://doi.org/10.5194/amt-8-611-2015>.
- Takayabu, Y. N., J. Yokomori, and K. Yoneyama, 2006: A diagnostic study on interactions between atmospheric thermodynamic structure and cumulus convection over the tropical western Pacific Ocean and over the Indochina Peninsula. *J. Meteor. Soc. Japan*, **84A**, 151–169, <https://doi.org/10.2151/jmsj.84A.151>.
- Waite, M. L., and B. Khouider, 2010: The deepening of tropical convection by congestus preconditioning. *J. Atmos. Sci.*, **67**, 2601–2615, <https://doi.org/10.1175/2010JAS3357.1>.
- Wentz, F. J., 2013: SSM/I version-7 calibration report. RSS Tech. Rep. 011012, 46 pp., [https://images.remss.com/papers/rsstech/2012\\_011012\\_Wentz\\_Version-7\\_SSMI\\_Calibration.pdf](https://images.remss.com/papers/rsstech/2012_011012_Wentz_Version-7_SSMI_Calibration.pdf).
- Windmiller, J. M., and C. Hohenegger, 2019: Convection on the edge. *J. Adv. Model. Earth Syst.*, **11**, 3959–3972, <https://doi.org/10.1029/2019MS001820>.
- Wodzicki, K. R., and A. D. Rapp, 2016: Long-term characterization of the Pacific ITCZ using TRMM, GPCP, and ERA-Interim. *J. Geophys. Res. Atmos.*, **121**, 3153–3170, <https://doi.org/10.1002/2015JD024458>.
- Xie, S.-P., 2004: The shape of continents, air–sea interaction, and the rising branch of the Hadley circulation. *The Hadley Circulation: Present, Past and Future*, H. F. Diaz and R. S. Bradley, Eds., Kluwer Academic Publishers, 121–152.
- , and S. G. H. Philander, 1994: A coupled ocean–atmosphere model of relevance to the ITCZ in the eastern Pacific. *Tellus*, **46A**, 340–350, <https://doi.org/10.3402/tellusa.v46i4.15484>.
- Zhang, C., M. McGauley, and N. A. Bond, 2004: Shallow meridional circulation in the tropical eastern Pacific. *J. Climate*, **17**, 133–139, [https://doi.org/10.1175/1520-0442\(2004\)017<0133:SMCITT>2.0.CO;2](https://doi.org/10.1175/1520-0442(2004)017<0133:SMCITT>2.0.CO;2).